Volume 1 | Number 1 | Jan 2013 | Pages 1–100

PCCP

Physical Chemistry Chemical Physics
www.rsc.org/pccp

ROYAL SOCIETY OF CHEMISTRY

ROYAL SOCIETY OF CHEMISTRY

www.rsc.org/pccp

Developing Functionalized Fe_3O_4-Au Nanoparticles:
a Physico-Chemical Insight

Alessandra Luchini [(a,b)], *Giuseppe Vitiello* [(b,c)], *Francesca Rossi* [(d)], *Odda Ruiz De Ballesteros* [(a)], *Aurel Radulescu* [(e)], *Gerardino D'Errico* [(a,b)], *Daniela Montesarchio* [(a)], *César de Julián Fernández* [(d)], *Luigi Paduano* *[(a,b)].

a Dipartimento di Scienze Chimiche, Università degli Studi di Napoli "Federico II", Complesso Universitario di Monte S. Angelo, via Cintia, 80126 Napoli, Italy.

b CSGI – Consorzio interuniversitario per lo sviluppo dei Sistemi a Grande Interfase, Italy.

c Dipartimento di Ingegneria Chimica, dei Materiali, e della Produzione Industriale, Università degli Studi di Napoli, "Federico II", Piazzale Tecchio 80, 80125 Napoli, Italy.

d Institute of Materials for Electronics and Magnetism – Italian National Research Council Parco Area delle Scienze 37/A - 43124 Parma, Italy.

e Jülich Centre for Neutron Science, Garching Forschungszentrum, Lichtenbergstrasse 1, D-85747 Garching bei München, Germany.

Nanotechnology for biomedicine is recently attracting increasing interest of the scientific community. In particular, among the different nanodevices suitable for this application, multifunctionalizable hybrid nanoparticles are one of the most investigated research topics. Here we present a detailed physico-chemical characterization of hybrid magneto-plasmonics iron oxide-gold nanoparticles (NPs) with core-shell structure. In particular, we underline all the synthetic difficulties concerning the preparation of these systems. Based on all our results, after different tests of a commonly reported protocol for the synthesis of the core-shell system, we believe that several issues are still open in the synthetic preparation of these particular NPs. Indeed, at least for the conditions that we adopted, core-shell morphology nanoparticles cannot be produced. However, independently from the core structure, we here describe an optimized and efficient functionalization protocol to obtain stable nanoparticle aqueous suspensions, which can be easily exported to other kinds of metal and metal-oxide NPs and aims to the development of biocompatible systems. Furthermore, reliable information that could be useful for researchers working in this field are extensively discussed.

1. INTRODUCTION

In nanomaterials field the combination of different inorganic and organic components in order to obtain biomaterials with novel or improved properties is one of the major research goals. Particularly, different synthetic protocols have been proposed to prepare metal and metal oxide nanoparticles coated with organic molecules. Indeed, by choosing the appropriate components, this kind of nanoparticles offers the possibility of combining different physical properties for the development of highly versatile systems.[1-3] In this context, Fe_3O_4 iron oxide nanoparticles are largely investigated as innovative contrast agents for Magnetic Resonance Imaging technique (MRI) [4], promising hyperthermia agents and drug delivery actuators[5, 6]. In particular, due to their magnetic properties, as contrast agents they act by shortening the T2 relaxation times of the protons located nearby, that in turn produce a darkening in the MRI image. In order to achieve early diagnosis of several pathologies, such as cancer, the development of novel and highly performing contrast agents is a mandatory task.[5, 7, 8]

One of the major concerns in the application of iron oxide nanoparticles in most biomedical applications is their still debated biocompatibility. For this reason many examples of functionalized and hybrid iron oxide nanoparticles have been described in the literature.[1, 9-13] In particular, iron oxide-gold nanoparticles with core-shell structure (named hereafter as NPs) are considered chemically stable and easily functionalizable systems, suitable for biomedical as well as bioanalytical applications.[14-17]. Moreover, the possibility to combine the different features and associated effects which the plasmonic (Au) and magnetic (Fe_3O_4) moieties exhibit, offers the opportunity to develop novel multifunctional nanodevices.[18, 19]

Taking inspiration from recently published scientific reports,[15, 20] we decided to implement a two-step thermal decomposition synthetic protocol in order to obtain a Fe_3O_4-Au core-shell platform with the aim of developing and optimizing an innovative and promising functionalization procedure. Our functionalization strategy is based on hydrophobic interactions and is therefore very general: it can thus be extended to all nanoparticles exposing an apolar stabilizing layer on their surface, and can exploit the aggregation properties of any amphiphilic compound to produce a double layer around the nanoparticles. In the present case, the second layer was formed by phospholipids, selected for their well recognized biocompatibility (Figure 1). This functionalization protocol is aimed at the optimization - in terms of biocompatibility - of the iron oxide-based nanoparticles as MRI contrast agents, and, furthermore, allows to introduce

amphiphilic drugs on the nanoparticle surface, thus being appropriate also for the development of theranostic devices. Indeed, there are very few examples in the literature of this kind of nanoparticle functionalization. In particular, amphiphilic molecules, such as the surfactant cetyltrimethylammonium bromide (CTAB) and lypopolysaccharides, [10, 21] have been proposed to build the second layer on nanoparticle surfaces, thus avoiding ligand exchange-based functionalization procedures. However, while CTAB is not considered biocompatible, the use of lypopolysaccharides resulted in functionalized nanoparticle suspensions characterized by a large value of the hydrodynamic radius. Though extremely innovative, both manuscripts do not report a description of the physical properties nor a detailed structural characterization of the analyzed systems.

In another contribution by Choi et al., gold nanoparticles were functionalized through hydrophobic interaction with a mixture of a short-chain phosphocholine, a modified PEG and an iminodiacetic acid succinyl nickel salt. This kind of nanoparticles has been designed to be water soluble and, at the same time, detectable by ferritin. [22]

In this work, an in-depth physico-chemical characterization of the nanoparticles obtained at each step of the synthesis, as well as of the functionalization procedure, is presented. During such characterization we faced with the need of combining several techniques, some of them having high resolution level, in order to fully understand the structure and composition of the prepared systems. As a matter of fact, functionalized NPs represent a complex system, since they include different, both organic and inorganic components, and the validation of the expected structure is extremely relevant. In this sense we have to underline that the most common structural characterization techniques can give ambiguous information and could lead to erroneous interpretations. The physico-chemical characterization of the prepared functionalized NPs was carried out in order to define the structural characteristics of the organic shell, which is formed on the nanoparticle surface through functionalization protocol, as well as of the inorganic core. The latter characterization studies pointed out that the products of several repeated syntheses were not showing the expected structure and composition for the inorganic core portion. Indeed the synthesis was repeated three times and the results here reported were always confirmed.

2. MATERIALS AND METHODS

2.1 NPs synthesis.

As largely reported in the literature[12, 15, 23, 24], nanoparticles with a core-shell structure can be produced through a two-step synthetic protocol based on thermal decomposition of metal salts. In this specific case we referred to the procedure described by Wang et al.[20]. According to this report, 0.355 g of iron(III) acetylacetonate (Fe(acac)$_3$, 99%), 1.29 g of 1,2-hexadecanediol (90%), 1.0 ml of oleylamine (OAM, 70%), 1.0 ml of oleic acid (OA, 99%) and 10 ml of diphenyl ether (99%), all purchased from Sigma Aldrich and used as received, were mixed together in a three-neck flask. The solution was heated at 200 °C under argon atmosphere and vigorous stirring. After 2 h at reflux, the flask was removed from the heater and cooled to room temperature. 5.0 ml of this solution were used for the successive synthetic step, and mixed with 0.415 g of gold(III) chloride trihydrate (Au(Cl)$_3$ ·3H$_2$O, 99%), also purchased from Sigma Aldrich, 1.55 g of 1,2-hexadecanediol, 0.25 ml of oleic acid, 1.5 ml of oleylamine and 15 ml of diphenyl ether. The resulting solution was heated at 200 °C under argon atmosphere and vigorous stirring, refluxed for 1.5 h, and then cooled to room temperature. The two synthetic steps are required to initially obtain the Fe$_3$O$_4$ nanoparticles, which are then used in the second step as seeds for the gold shell deposition.

1,2-hexadecanediol was chosen as reducing agent to convert in the first step the iron(III) salts in the Fe$_3$O$_4$ oxide, containing both Fe(II) and Fe (III), as well as for the reduction of the gold salt during the second step, while oleic acid and oleylamine were introduced as stabilizing agents to prevent nanoparticle aggregation.

At the end of the synthesis, in order to remove the undesired components, such as excess of iron oxide nanoparticles non-coated with the gold shell, the suspension was treated with ~ 10 ml of ethanol and centrifuged at 7000 rpm for 20 min. The nanoparticles, obtained as a solid precipitate, have been then redispersed in cyclohexane.

The iron concentration in the synthesis product was evaluated by means of Inductively Coupled Plasma Mass Spectroscopy (ICP-MS) as corresponding to 0.05 mg/ml.

2.2 NPs functionalization protocol.

The thermal decomposition method leads to a nanoparticle suspension stable in organic solvents. However, for biomedical applications suspensions equally stable in water solutions are needed and, thus, a proper functionalization procedure is essential to improve their stability in aqueous media. In addition, in order to avoid further purification steps and loss of the synthesis product, it would be desirable to conceive a single step protocol for such functionalization.

In order to satisfy all these queries, and above all to handle an extremely versatile functionalization strategy, we developed the here described protocol. In particular, by exploiting the hydrophobic tails of oleic acid and oleylamine decorating the nanoparticle surface, a second layer of amphiphilic molecules was deposited on it (Figure 1). Thus, the design of our functionalized NPs is composed by an inorganic nanoparticle with core-shell structure covered by two layers of organic molecules. The second layer is responsible for the stability in water media and can lodge additional amphiphilic molecules with specific properties, thus producing a multifunctional system.

— Oleic acid and oleylamine

— 1-stearoyl-2-hydroxy-*sn*-glycero-3-phosphocholine (18LPC)
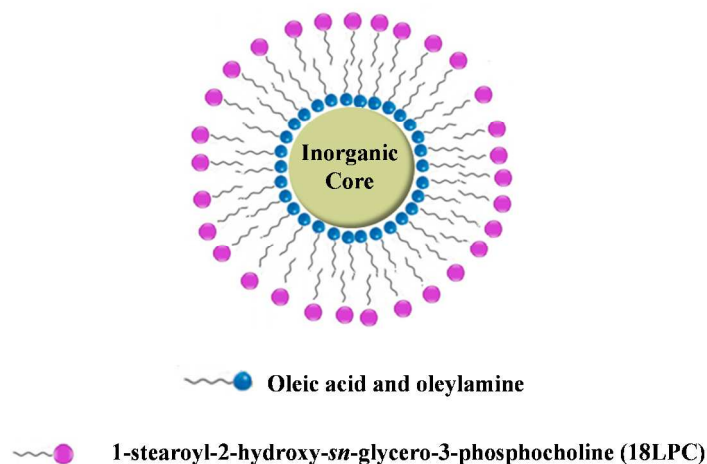
Figure 1: Schematic representation of the here described nanoparticle structure.

In particular, if biocompatible surfactants, such as phospholipids, are used, the functionalized nanoparticle suspension, in principle, presents a lower toxicity. Furthermore, a mixture of biocompatible molecules and amphiphilic drugs can produce novel theranostic agents. In the latter case the drug is reversibly bound to the nanoparticle surface and once in vivo can be easily released to explicate its activity.

In order to prepare functionalized NPs, according to the previously described strategy, 1.0 ml of the nanoparticle suspension in cyclohexane was stratified over 1.0 ml of an aqueous solution containing biocompatible lipids, purchased from Avanti Polar Lipids. In particular 1-palmitoyl-2-hydroxy-*sn*-glycero-3-phosphocholine (16LPC 99%), or 1-octadecyl-2-hydroxy-*sn*-glycero-3-phosphocholine (18LPC 99%) at $4.0 \cdot 10^{-3}$ molal concentration were used. Bath sonication of the biphasic system at 50 °C for about 2 h promoted the cyclohexane evaporation and the transfer into the aqueous phase of the nanoparticles decorated with a layer of 16LPC or 18LPC, hereafter indicated as 16LPC/NPs and 18LPC/NPs (Figure 1). The chosen phospholipids differ for their hydrocarbon chain length that should influence the compactness of the layer on the nanoparticles surface.

A second sonication step with a tip-sonicator, composed of at least 5 cycles, each of 1 min, in order to avoid the overheating of the suspension, was also introduced to ensure the obtainment of nanoparticle suspension with reproducible size-distribution.

The here reported functionalization protocol can be easily exported to any molecule with amphiphilic structure and thus exploited in a large variety of applications of nanoparticles. Furthermore, it only requires that the nanoparticle surface exposes an apolar tails layer, and since several inorganic nanoparticle synthetic protocols include the use of long chain stabilizing agents, the proposed strategy can be adopted to functionalize nanoparticles constituted of different metal oxides. Another relevant advantage is that the functionalization procedure is a one-step protocol, which does not require further purification.

2.3 Dynamic Light Scattering (DLS)

DLS measurements were performed with a home-made instrument composed by a Photocor compact goniometer, a SMD 6000 Laser Quantum 50 mW light source operating at 5325 Å, a photomultiplier (PMT-120-OP/B) and a correlator (Flex02-01D) from *Correlator.com*.[25] The measurements were performed at (25.00 ± 0.05) °C with temperature controlled through the use of a thermostat bath. All experiments were performed at the scattering angle of 90° (θ), the value of the scattering vector $q = 4\pi n / \lambda \sin(\theta / 2)$ was calculated assuming the refractive index of the solution n= 1.33 for the water suspension and n = 1.43 for the cyclohexane suspension. The scattered intensity correlation function was analyzed using a regularization algorithm.[26] The

measured diffusion coefficients was taken as the z-average diffusion coefficient of the obtained distributions.[27]

For spheres diffusing in a continuum medium at infinite dilution, the diffusion coefficient $\langle D \rangle \equiv \langle D \rangle_\infty$, and is dependent on the sphere radius R_H, called hydrodynamic radius, through the Stokes–Einstein equation:

$$R_H = \frac{kT}{6\pi\eta\langle D_\infty \rangle} \tag{3}$$

where k is the Boltzmann constant, T is the absolute temperature and η is the medium viscosity, assumed to be 0.89 cP for the water suspension and 1.02 cP for the cyclohexane suspension. For not spherical particles, R_H represents the radius of equivalent spherical aggregates. In this hypothesis, equation (3) can be reasonably used to estimate the averaged hydrodynamic radius of the aggregates.[28]

In the present case the R_H was estimated from at least three measurements of the diffusion coefficients of the aggregates for each analyzed samples.

2.4 Small Angle Neutron Scattering (SANS)

SANS measurements were performed at 25 °C with the KWS2 instrument located at the Heinz Meier Leibtnitz Source, Garching Forschungszentrum (Germany).[29] Neutrons with a wavelength spread $\Delta\lambda/\lambda \leq 0.2$ were used. A two-dimensional array detector at three different wavelength (W)/collimation (C) /sample-to-detector(D) distance combinations ($W_{7Å}C_{8m}D_{2m}$, $W_{7Å}C_{8m}D_{8m}$ and $W_{19Å}C_{8m}D_{8m}$), measured neutrons scattered from the samples. These configurations allowed collecting data in a range of the scattering vector modulus $q = 4\pi/\lambda \sin(\theta/2)$ between 0.0019 $Å^{-1}$ and 0.179 $Å^{-1}$, with θ scattering angle. The investigated systems were contained in a closed quartz cell, in order to prevent the solvent evaporation and kept under measurements for a period sufficient to have ~ 2 million counts. Measurements at very small angle were performed at KWS3 running on the focusing mirror principle at the Research Neutron Source Heinz-Maier Leibnitz (FRM-II) in Garching (Germany). Standard configuration of the instrument with 9.5 m

sample-to-detector distances allows performing scattering experiments with a wave vector transfer resolution between 10^{-4} and $3 \cdot 10^{-3}$ Å^{-1}, bridging a gap between Bonse-Hart and pinhole cameras. Second sample position at 1.3 m distances has extended Q-range of the instrument to 2 10^{-2} Å^{-1} and reached more than one-decade overlapping with the classical pinehole SANS instruments. The principle of this instrument is a one-to-one image of an entrance aperture onto a 2D position sensitive detector by neutron reflection from a double-focusing toroidal mirror. The raw data were then corrected for background and empty cell scattering. Detector efficiency correction, radial average and transformation to absolute scattering cross sections $d\Sigma/d\Omega$ were made with a secondary plexiglass standard[30, 31].

Thus, the so obtained absolute scattering cross sections $d\Sigma/d\Omega$ data were plotted as function of q. Generally, the dependence of $d\Sigma/d\Omega$ from the scattering vector can be summarized as in equation 3:

$$\frac{d\Sigma}{d\Omega} = n_p P(q)S(q) + \left(\frac{d\Sigma}{d\Omega}\right)_{incoh} \tag{3}$$

where n_p is the number of scattering objects, *P(q)* and *S(q)* are respectively the form factor and the structure factor, and the last term takes into account the incoherent scattering mostly due to the presence of hydrogen atoms within the sample.

The form factor is responsible for the shape, size distribution of the scattering particles, while a contribution of the structure factor can be considered when an interparticle correlation exists. The structural information contained in both the form and the structure factor can be extrapolated by choosing an appropriate model to fit the obtained experimental data.[32]

2.5 Electron Paramagnetic Resonance (EPR)

EPR spectra were recorded on a 9 GHz Bruker Elexys E-500 spectrometer (Bruker, Rheinstetten, Germany). Capillaries containing 200 µl of the samples were placed in a standard 4 mm quartz sample tube containing light silicone oil for thermal stability. The temperature of the sample was regulated at 25 °C and maintained constant during the measurement by blowing thermostated nitrogen gas through a quartz Dewar. The instrumental settings were as follows: sweep width,

6000 G; resolution, 1024 points; modulation frequency, 100 kHz; modulation amplitude, 1.0 G; time constant, 20.5 ms, incident power, 6.4 mW, Gain 60 dB. 64 scans were accumulated to improve the signal-to-noise ratio.

2.6 Magnetic characterization

The hysteresis loops were recorded at room temperature using an Alternating Gradient Force Magnetometer (Model 2900, Princenton Measurements Corporation), while the hysteresis loops at low temperatures, 10 K, and the temperature dependence of the magnetization were measured using a SQUID magnetometer (Mod. XMPS-XL, Quantum Design). In particular, the temperature dependence of the magnetization was recorded using the procedure of Zero-field-cooling (ZFC) and Field Cooling (FC). The ZFC measurements were carried out by cooling the sample in zero magnetic field from room temperature to 10 K. Then a small magnetic field of 100 Oe was applied and the magnetization was measured while the temperature was raised up to room temperature. For the FC measurement the sample was cooled again to 10 K, this time under a magnetic field, and as for the ZFC measurement, the magnetization data were collected as function of the temperature. All the magnetic moments were normalized to the magnetization *per* dried sample mass.

2.7 Wide Angle X-ray Scattering (WAXS)

The X-ray diffraction profiles were obtained with Ni-filtered Cu Kα radiation ($\lambda = 1.5418$ Å) by using an automatic Philips diffractometer. The profiles were recorded performing a step scan of the diffraction angle 2θ in the range 20 - 70° with a step size of 2θ equal to 0.1 ° and a time per step of 14.3 s. The Pulse Height Distribution (PHD) level values of the detector were set to 35 and 80% for the lower and upper level, respectively, to reduce the background intensity due to the fluorescence of the samples.

2.8 Transmission Electron Microscopy (TEM)

Transmission Electron Microscopy analyses were performed in a JEOL JEM 2200FS Field-Emission microscope, equipped with in-column Omega filter, working at 200 kV. The microscope was operated in Scanning (STEM) mode to acquire High Angle Annular Dark Field (HAADF) images, based on Z-contrast principles[33], and Energy Dispersive X-ray (EDX) spectra and related elemental maps. The probe size was set to 1 nm.

3. RESULTS AND DISCUSSION

This physico-chemical characterization of the NPs shell aimed to validate the proposed functionalization protocol as a useful method to induce nanoparticle water stability, as well as potential improved biocompatibility.

DLS analysis showed that the nanoparticles cyclohexane suspension (Fe_3O_4 coated with oleic acid and oleylamine), obtained from the thermal decomposition method, is composed by a single and very narrow population having the mean hydrodynamic radius of (8 ± 2) nm. The suspension show long time stability and even after several weeks no precipitation is observed. This is consistent with the typical nanoparticle size provided by this type of synthetic approach (Figure 2, panel a).[15, 20] From this suspension a further coating of the NPs with lipid molecules was attained.

The functionalized NPs are composed by an inorganic core and organic shell; thus, in order to have a detailed characterization of the structure and composition of both portions, it was necessary to combine several techniques, suitable for probing the different nanoparticle components.

3.1a Functionalized NPs shell characterization.

The functionalized NPs are characterized by the presence on their surface of an additional amphiphilic layer, in the present case composed by the phospholipid 18LPC (data concerning the 16LPC functionalization are reported in the SI section) that led to the formation of 18LPC/NPs. In order to detect the formation of this additional layer, with respect to the first one already present on the NPs surface composed by oleic acid and oleylamine, DLS and SANS measurements were performed.

The hydrodynamic radius distribution changed significantly upon nanoparticle transfer into aqueous suspensions, as a result of their additional coating. The 18LPC/NPs system exhibits a single broaden distribution whose mean hydrodynamic radius is about 30 nm. Indeed, as we will see below, small-angle neutron scattering experiments pointed out that both 16LPC/NPs (Figure SI1) and 18LPC/NPs system are characterized by a bimodal distribution (i.e. two aggregate populations of different size are present in the system). However in the 18LPC/NPs the

difference in size of the two populations is quite small so they appear as a single broad peak. In obtaining a separation of the two contributions regularization process of the DLS correlation function does not allow a reproducible result.[26]
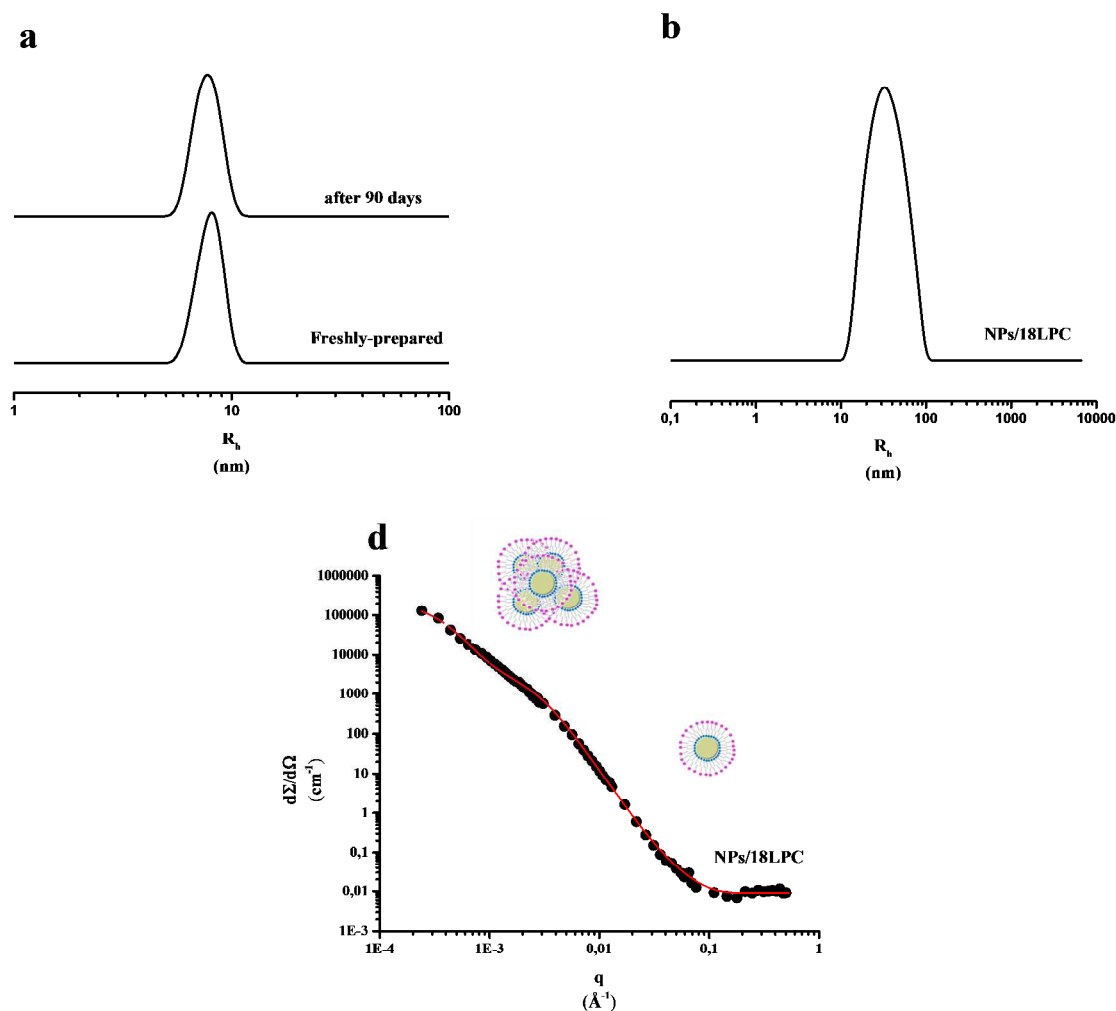
Figure 2: Hydrodynamic radius distributions of nanoparticle suspension in cyclohexane with Fe concentration corresponding to 0.05 mg/ml (panel a), as well as 18LPC functionalized nanoparticle water suspensions with Fe concentration 0.04 mg/ml (panel b). Neutron scattered intensity profiles obtained for 18LPC functionalized nanoparticles (panel c); the region where clusters and single functionalized contributions are prevalent is indicated.

The neutron scattering intensity profiles (Figure 2, panel c) were modelled combining two different form factors in order to take into account the contribution arising from the nanoparticle clusters as well as the single functionalized nanoparticles. Since the nanoparticle clusters contribution reaches out low q values, the two profiles obtained from SANS and VSANS experiments were superimposed. The whole curve was then fitted considering the system as

constituted by single core-shell nanoparticles and large homogenous spheres, the latter being the NPs clusters. In such a way an evaluation of the cluster size was possible, according to the following equations:

$$I(q) = \varphi_{core-shell}P_{core-shell} + \varphi_{cluster}P_{cluster} + bkg \tag{8}$$

with

$$P_{core-shell}(q) = \frac{scale}{V_{sphere}}\left[3V_c(\rho_c-\rho_s)\frac{\sin(qr_c)-qr_c\cos(qr_c)}{qr_c}+3V_s(\rho_s-\rho_{solv})\frac{\sin(qr_s)-qr_s\cos(qr_s)}{qr_s}\right] \tag{9}$$

and

$$P_{cluster}(q) = \frac{scale}{V_{cluster}}\left[3V_{cluster}(\rho_{cluster}-\rho_{solv})\frac{\sin qr_{cluster}-qr_{cluster}\cos(qr_{cluster})}{qr_{cluster}}\right] \tag{10}$$

In the case of the core-shell form factor, the core was considered as formed by both iron oxide and gold, while the organic layers, which are present on the nanoparticle surface, constitute the shell. Indeed, the scattering length density of gold and Fe_3O_4 iron oxide was calculated to be respectively $4.5\cdot10^{-6}$ Å^{-2} and $6.9\cdot10^{-6}$ Å^{-2}. Thus, the contrast between these two components was not sufficient to distinguish them using neutron scattering.

As summarized in Table 1, the single functionalized nanoparticles resulted to have the inorganic core (Fe_3O_4-Au) radius together with the organic shell thickness in good agreement with the values obtained from DLS measurements.

	$R_{h,NPs}$ (nm)	$R_{h,cluster}$ (nm)	R_{core} (nm)	d (nm)	$R_{cluster}$ (nm)
18/LPC	(29 ± 1)		(5.5 ± 0.5)	(4.0 ± 0.4)	(45 ± 1)

Table 1: *Hydrodynamic radius values obtained from DLS analysis and core radius and organic shell thickness obtained from SANS experiments. $R_{h,NPs}$ indicates the hydrodynamic radius of the single functionalized nanoparticle and $R_{h,cluster}$ is the hydrodynamic radius of the cluster. Furthermore, R_{core} is the inorganic nanoparticle radius, d is the thickness of the organic coating and $R_{cluster}$ is the radius of the cluster.*

DLS and SANS characterization confirmed that the functionalized NPs were stable in aqueous media thanks to the formation of an organic coating composed by two amphiphilic layers. Furthermore, a certain tendency of the functionalized NPs to form clusters was also detected (see SI section). In particular, the more hydrophobic 18LPC produces a more efficient and compact

layer on the nanoparticle surface with respect to 16LPC, thus reducing the clustering propensity of 18LPC/NPS with respect to 16LPC/NPS. This effect could represent an appropriate tool to tailor functionalized nanoparticle systems toward a specific size distribution.

3.2b Functionalized NPs core characterization.

In a second part of this work we focus on the structure of the inorganic core. As well as the aggregation behaviour, also the composition-structure relationships of the synthesized nanoparticles are fundamental to verify the achievement of an effective contrast agent and a potentially theranostic device. By investigating the composition-structure relationships we intend to confirm the simultaneous presence within the nanoparticles of both Fe_3O_4 iron oxide and gold (composition) in form of a core-shell system (structure). Controlling the composition is essential, especially for the iron-oxygen stoichiometric ratio in the synthesized iron oxide. Exclusively the net magnetic moment due to the ferrimagnetism and the single domain structure of the Fe_3O_4 iron oxide nanoparticles makes these nanoparticles suitable contrast agents for Magnetic Resonance Imaging (MRI).

In order to verify the inorganic core composition and its core-shell structure, we combined Wide Angle X-ray Scattering (WAXS), Electron Paramagnetic Resonance (EPR), high-resolution Transmission Electron Microscopy (TEM) and magnetometry techniques. In this characterization the iron oxide nanoparticle suspension (named hereafter as suspension 1) was compared to the bilayer-decorated nanoparticle suspension obtained at the end of the entire functionalization procedure (named hereafter as suspension 2).

Nanoparticles thin films suitable for WAXS measurements were obtained by drop casting of suspensions 1 and 2 on a glass side. The X-ray diffraction profiles of these films are reported in Figure 3. The values of the diffraction angles (2θ), Bragg distances (*d*), relative intensities (*I*) and Miller indices (*hkl*) of the reflections observed in the profiles of Figure 3 are listed in Table 2.

The diffraction profile of the nanoparticle film obtained by suspension 1 shows a strong peak at $2\theta = 35.4°$ and less intense peaks at $2\theta = 30, 43.1, 57$ and $62.6°$ (panel a of Figure 3), corresponding to the 311, 220, 400, 511 and 440 reflections, respectively, of the crystalline structure of Fe_3O_4 iron oxide.[34] This clearly demonstrates that the adopted synthetic procedure allows to obtain magnetite Fe_3O_4 nanoparticles.

The diffraction profile of the nanoparticle film prepared by suspension 2 is characterized by the presence of three peaks at $2\theta = 38.2$, 44.4 and 64.6° (panel b of Figure 3), corresponding to the 111, 200 and 220 reflections of the crystalline structure of gold.[35] Diffraction peaks corresponding to the crystalline structure of Fe_3O_4 are not detectable in the diffraction profile of suspension 2.

The presence of the sole reflections typical of the crystalline structure of gold has been interpreted by many authors as an evidence of the formation of compact gold shell on the iron oxide core.[20] However, this finding alone is not conclusive and indeed three major morphologic configurations could be hypothesized to explain these results. Hypothesis 1): only gold nanoparticles are present after gold salt reduction because iron oxide nanoparticles undergo degradation; hypothesis 2): the synthesis product is a mixture of gold and iron oxide nanoparticles, but the diffraction contribution from gold dominates and overlays the diffraction peaks of iron oxide; hypothesis 3): the synthesis product is effectively a core-shell system in which the gold shell shields the iron oxide core from X-rays and, thus, only diffraction peaks of gold are observable. Therefore, further characterization techniques are necessary to fully demonstrate the presence of a core-shell system.
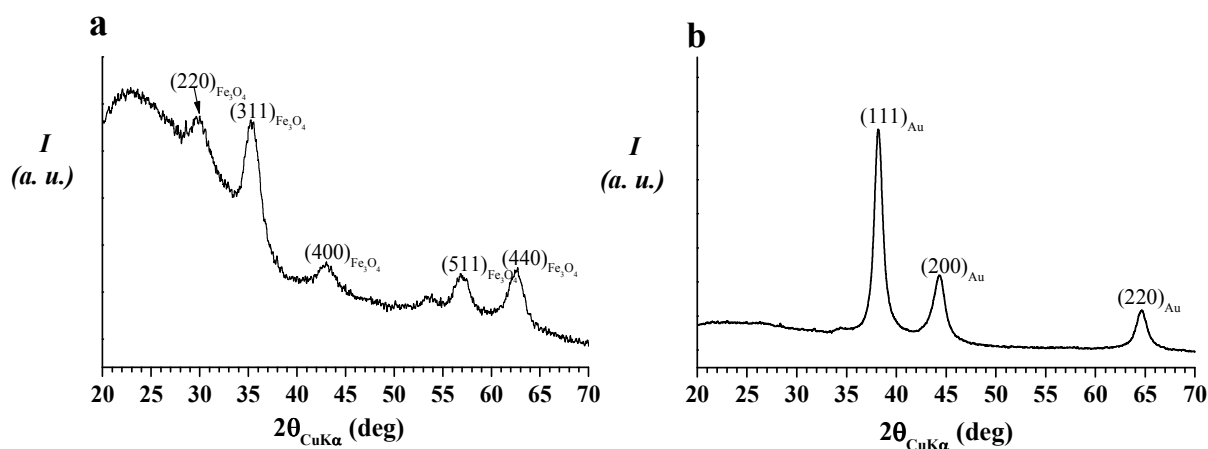
Figure 3: Wide angle X-ray diffraction profiles of nanoparticles thin films obtained by suspension 1 (panel a) and suspension 2 (panel b). The Miller indices of Fe_3O_4 and gold (Au) reflections are indicated.

Suspension 1 (iron oxide nanoparticles)				Suspension 2 (iron oxide-gold nanoparticles)			
$2\theta_{CuK\alpha}$ (deg)	d (Å)	I	hkl	$2\theta_{CuK\alpha}$ (deg)	d (Å)	I	hkl
30.0	2.97	30	220	38.2	2.35	100	111
35.4	2.53	100	311	44.4	2.04	52	200
43.1	2.10	20	400	64.6	1.44	32	220
57.0	1.62	30	511				
62.6	1.84	40	440				

Table 2: *Diffraction angles (2θ), Bragg distances (d), relative intensities (I) and Miller indices (hkl) of the diffraction peaks observed in the diffraction profiles of Figure 3 panels a and b.*

a

b
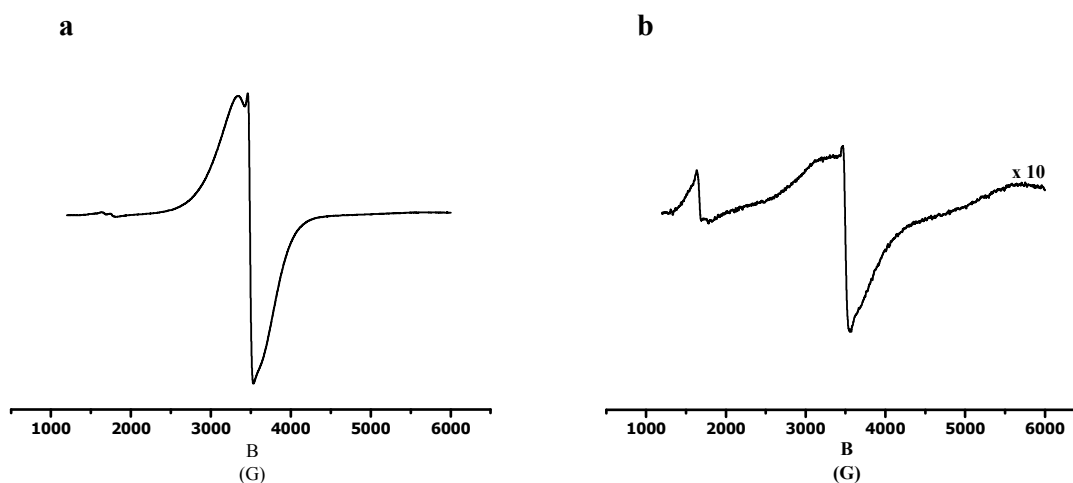
Figure 4: *EPR spectra for 1:100 diluted suspension 1 with Fe concentration 0.02 mg/ml (panel a) and suspension 2 with Fe concentration 0.05 mg/ml (panel b).*

EPR spectra were collected for both nanoparticles suspensions 1 and 2. In particular, suspension 1 was diluted 1:100, to reduce the signal intensity. The iron concentration in diluted suspension 1 and in suspension 2 - evaluated through Inductively Couples Plasma- Mass Spectroscopy (ICP-MS) measurements - resulted to be respectively 0.238 mg/ml and 1.64 mg/ml.

As well known, only paramagnetic or magnetic species can produce an EPR signal, and if Fe_3O_4 were present within the analysed suspensions a typical signal centred at 3500 G should be observed.[36] In Figure 4 the resulting spectra are reported, and, as it is possible to observe, the previously indicated signal is evident in both cases. Thus, qualitative EPR analysis confirmed

that suspension 2 is not composed by pure gold nanoparticles (hypothesis 1). Furthermore, even if the iron concentration was higher in suspension 2, the corresponding spectrum resulted to be less intense of about a factor 10 with respect to the one obtained for the diluted suspension 1. This result suggests that reasonably the two suspensions contained a greatly different amount of iron oxide nanoparticles. On the other hand, from the collected data the effective presence of Fe_3O_4 could not be detected, since different iron oxides and even iron complexes are able to produce the observed EPR signal.[1]
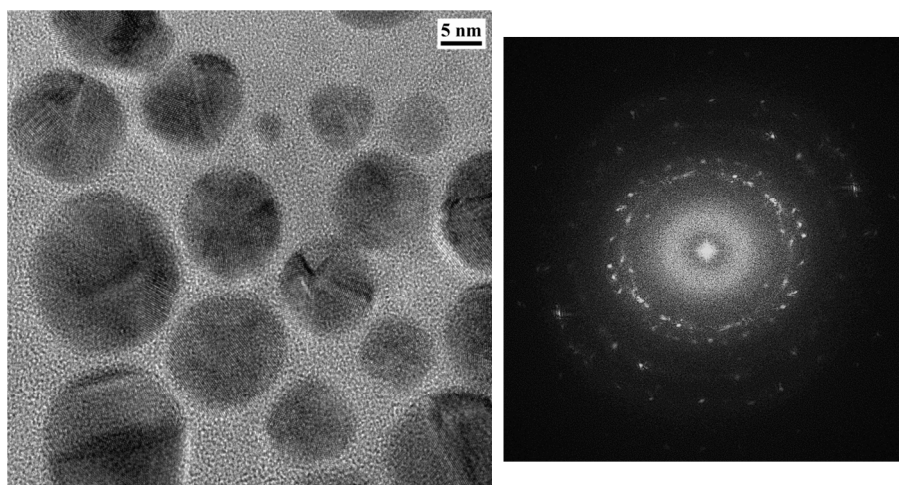
Figure 5: *HRTEM image of the suspension 2 (left panel) and the corresponding Fast Fourier Transform (right panel).*

TEM studies were fundamental to clarify the composition and structure of the synthesized nanoparticles, and to overcome the ambiguities arising from the results obtained through the typical physico-chemical characterization techniques. Figure 5 shows a representative High Resolution Transmission Electron Microscopy (HRTEM) image, and the corresponding Fast Fourier Transform (FFT), of the NPs. The size distribution of the nanoparticles contained in suspension 2 is quite spread, being about (10 ± 7) nm. The FFT shows a first ring at d=0.235 nm,

---

[1] *In the spectrum corresponding to suspension 2, also a narrow line around 1500 G was detected. This line corresponds to a g = 4.3, that is a high spin Fe(III) in low symmetry. 37.   F. Bou-Abdallah and N. D. Chasteen, J Biol Inorg Chem, 2008, 13, 15-24. Actually, another possibility is that it corresponds to a forbidden transition ΔM±2 that has been observed in Fe- oxide clusters in ferritine cage36.   M. M. Noginov, N. Noginova, O. Amponsah, R. Bah, R. Rakhimov and V. A. Atsarkin, J Magn Magn Mater, 2008, 320, 2228-2232, 38.   M. Fittipaldi, C. Innocenti, P. Ceci, C. Sangregorio, L. Castelli, L. Sorace and D. Gatteschi, Phys Rev B, 2011, 83. However, independently of the assignment, the observation of this secondary line suggests the presence of other phases in addition to the Fe oxide NPs if any in suspension 2.*

corresponding to the (111) fringes of gold, and two inner spots at d=0.32 nm. No larger lattice periodicities are seen, indicating that the expected iron oxide reflections are not present.
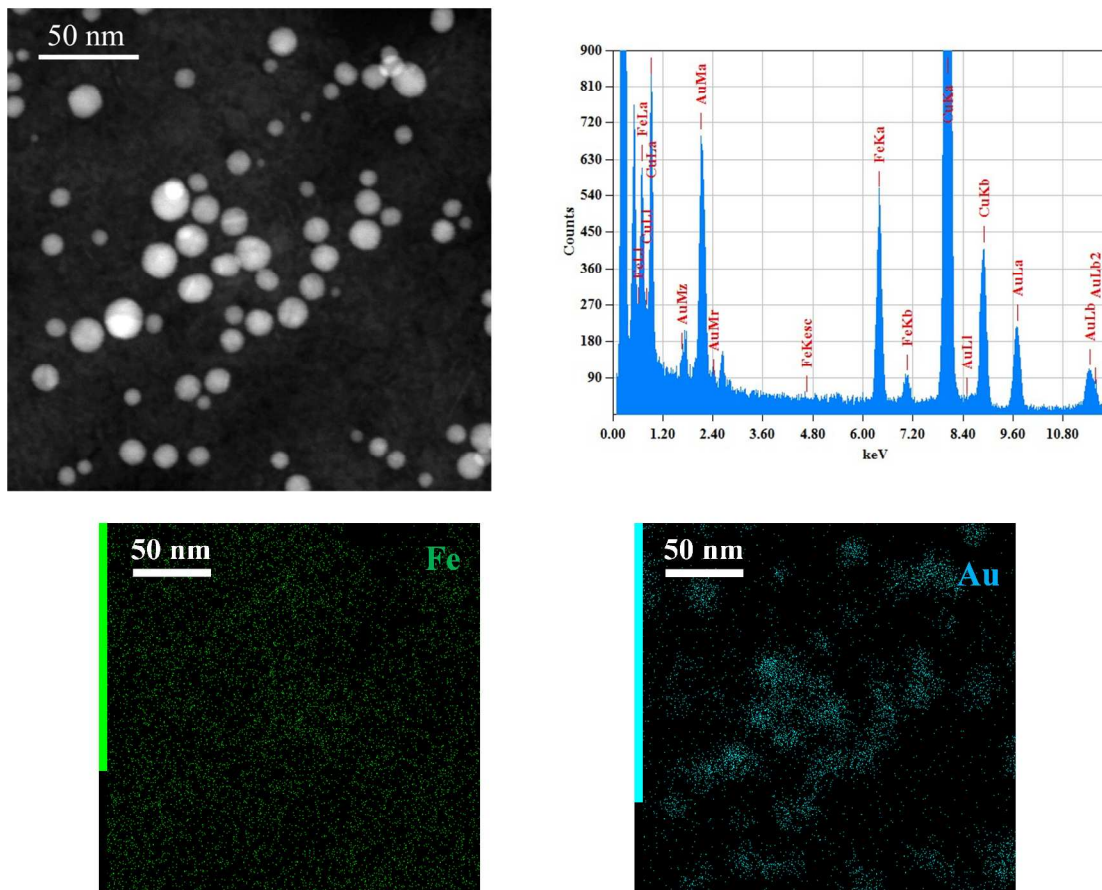
Figure 6: STEM-HAADF image of suspension 2 (on left-top)together with the corresponding EDX spectrum (on right top) and the elemental maps referring to Fe-K (on left-bottom)and Au-M (on right-bottom) edges.

Figure 6 shows a representative STEM-HAADF image of a NPs ensemble and the corresponding EDX spectrum and elemental maps obtained selecting the Au-M and Fe-K edges. As can be observed, no intra-particle Z-contrast related to a core-shell structure is observed. The EDX maps confirm that all the observed NPs are composed of gold, while iron is widely distributed and does not form particles or shells. These results suggest that iron is present in the system but more likely dispersed like ions or clusters and that instead of producing a gold shell, the second thermal decomposition led to the formation of independent gold nanoparticles.

At this point we were able to completely exclude hypothesis 3), but in order to discriminate between 1) and 2), and to finally define if Fe-oxide survives to the second synthesis step, the

magnetic properties of the nanoparticles were analysed. Indeed, TEM studies allow to obtain detailed information on small aliquots of sample while magnetic characterization always concerns higher amount of material.

The magnetic properties of the powders relative to suspension 1 and suspension 2 (Figure 7, panels a and b) were investigated. The room temperature hysteresis of suspension 1 exhibits an s-shape curve typical of superparamagnetic nanoparticles with a magnetization saturation (M_s) value of 15 emu/g. This value, if related to the typical bulk M_s of magnetite, which corresponds to 80 emu/g, suggests the presence of about 17% of magnetic materials. Roughly, the same result is obtained calculating the percentage of iron oxide in the solid material from the iron concentration of 3.4 mg/ml, analysed by means of ICP-MS. This calculation indicates that all the iron oxide contained in suspension 1 is in form of magnetite Fe_3O_4. On the other hand, suspension 2 produced a completely different hysteresis loop (figure 7, panel b). Indeed, the continuous increase of the magnetization at high fields, without reaching saturation, indicates that, together with the superparamagnetic nanoparticles, also some paramagnetic or spin-glass species are present. Subtracting the paramagnetic contribution, the total magnetic magnetization of the superparamagnetic component in suspension 2 is almost two order of magnitude smaller than that of suspension 1. At low temperature, 10 K, the hysteresis loop of suspension 2 (not shown) shows mainly an unsaturated magnetic field dependence, typical of paramagnetism or antiferromagnetism but certain hysteresis is observed without the possibility to separate these contributions.

In the case of suspension 1, the low temperature hysteresis loop exhibits the classical shape of blocked nanoparticles with coercive fields of 100 Oe. The temperature dependence of the magnetization, using the ZFC - FC (Figure 7, panel c) methodology, was measured to investigate the superparamagnetic behaviour of both nanoparticles suspensions. In the case of suspension 1, the transition from low-temperature blocking behaviour to high temperature superparamagnetic behaviour[39] occurs in a narrow temperature range with the average blocking temperature (T_B) of 30 K, corresponding to the maximum of the ZFC magnetization. On the other hand, in the case of suspension 2 the average blocking temperature is much smaller, 12 K (Figure 7, panel d). The blocking temperature is proportional to the effective magnetic anisotropy of the nanoparticles and to their average volume. The observed differences in the blocking temperature of the two suspensions confirmed the differences of the magnetic properties of the nanoparticles that

compose the two suspensions. However, comparing the overall magnetic results obtained for suspension 1 and 2, we concluded that only a small amount of Fe_3O_4 iron oxide, but with different features, is still present in the nanoparticle suspension after the second thermal decomposition. This result is in agreement with the observation reported in the literature that the introduction of gold generally produces a considerable reduction of the magnetic properties of the nanoparticle suspension[20].
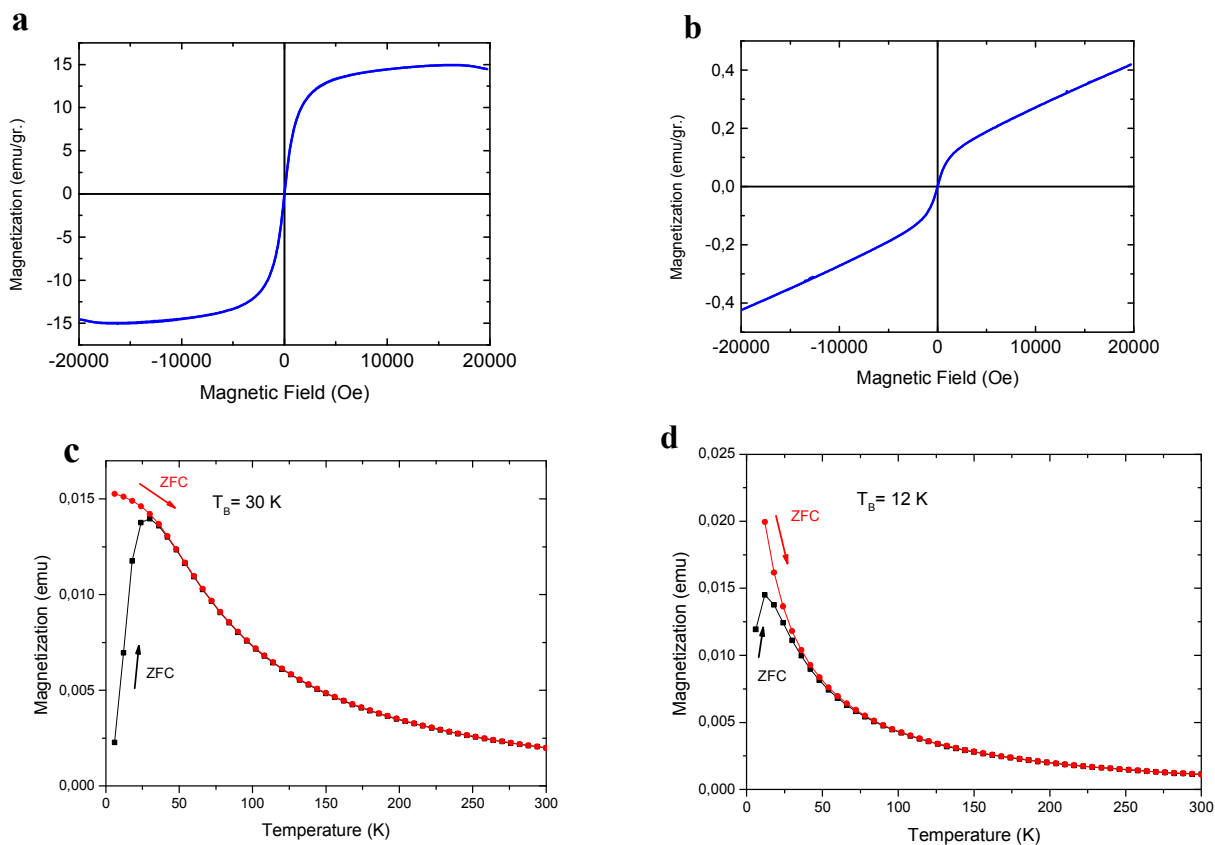
Figure 7: Hysteresis loops for suspension 1 (panel a) and suspension 2 (panel b) powders; evaluation of the blocking temperature using ZFC-FC methodology for suspension 1 and suspension 2 powders (respectively panel c and d).

CONCLUSIONS.

The presented work aimed to introduce a novel class of functionalized iron oxide-gold nanoparticles for biomedical applications as effective contrast agents for Magnetic Resonance

Imaging, and at the same time as suitable nanocarriers in view of developing efficient theranostic devices. Indeed, we demonstrated the feasibility of our functionalization approach, based on a hydrophobic coating of the inorganic nanoparticles - required for their stabilization - followed by decoration with a second amphiphilic layer composed by a phoshocholine.

The detailed characterization of both the organic and inorganic components of the functionalized nanoparticles led to conclude that: 1) stable functionalized nanoparticles suspensions in water were achieved with a controlled size distribution; 2) the size of the functionalized nanoparticles and more specifically the potential formation of nanoparticle clusters is strictly connected to the phosphocholine CMC, i.e. its aggregation tendency; 3) all the data collected to investigate the structure and the composition of the nanoparticle inorganic core indicated that the here adopted synthetic protocol led to a mixture of mainly gold nanoparticles and a small amount of Fe_3O_4 iron oxide nanoparticles, instead of the expected core-shell system.

We believe that our experience should push researchers working in this field to be very careful in the interpretation of the characterization data, also taking into account that the combination of several, different techniques is fundamental in order to fully verify the obtainment of a core-shell system such as the iron oxide-gold one.

Even if we did not obtain the desired core-shell nanoparticles, our results pointed out that the here described functionalization protocol was perfectly effective with both gold and iron oxide nanoparticles - unconsciously present as a mixture in the tested nanoparticle suspensions. It can be thus concluded that this functionalization strategy is very versatile, being essentially independent on the nanoparticle composition, and only requires that the nanoparticles expose on their surface a hydrophobic layer.

On this basis, our future efforts in this field will be directed to the preparation of simple iron oxide-based nanoparticles decorated with different amphiphilic compounds so to ensure multifunctional devices for both diagnostic and therapeutic purposes.

AUTHOR INFORMATION.

Corresponding Author:

* E-mail: luigi.paduano@unina.it

Present address:

Dipartimento di Scienze Chimiche, Università degli Studi di Napoli "Federico II", Complesso Universitario di Monte S. Angelo, via Cintia, 4, 80126 Naples, Italy.

REFERENCES.

1.   M. B. Cortie and A. M. McDonagh, *Chem Rev*, 2011, 111, 3713-3735.

2.   Y. M. Zhai, L. Han, P. Wang, G. P. Li, W. Ren, L. Liu, E. K. Wang and S. J. Dong, *ACS Nano*, 2011, 5, 8562-8570.

3.   U. Banin, Y. Ben-Shahar and K. Vinokurov, *Chem Mater*, 2014, 26, 97-110.

4.   M. K. Yu, J. Park and S. Jon, *Theranostics*, 2012, 2, 3-44.

5.   J. M. Knipe, J. T. Peters and N. A. Peppas, *Nano Today*, 2013, 8, 21-38.

6.   M. E. Caldorera-Moore, W. B. Liechty and N. A. Peppas, *Acc Chem Res*, 2011, 44, 1061-1070.

7.   M. Vaccaro, G. Mangiapia, A. Radulescu, K. Schillen, G. D'Errico, G. Morelli and L. Paduano, *Soft Matter*, 2009, 5, 2504-2512.

8.   A. Accardo, P. Ringhieri, N. Szekely, V. Pipich, A. Luchini, L. Paduano and D. Tesauro, *Colloid Polym Sci*, 2014, 292, 1121-1127.

9.   K. Turcheniuk, A. V. Tarasevych, V. P. Kukhar, R. Boukherroub and S. Szunerits, *Nanoscale*, 2013, 5, 10729-10752.

10.   R. Hao, R. J. Xing, Z. C. Xu, Y. L. Hou, S. Gao and S. H. Sun, *Adv Mater*, 2010, 22, 2729-2742.

11.   A. H. Lu, E. L. Salabas and F. Schuth, *Angew Chem Int Edit*, 2007, 46, 1222-1244.

12.   R. G. Chaudhuri and S. Paria, *Chem Rev*, 2012, 112, 2373-2433.

13.   L. Carbone and P. D. Cozzoli, *Nano Today*, 2010, 5, 449-493.

14.   C. S. Levin, C. Hofmann, T. A. Ali, A. T. Kelly, E. Morosan, P. Nordlander, K. H. Whitmire and N. J. Halas, *ACS Nano*, 2009, 3, 1379-1388.

15.   Z. C. Xu, Y. L. Hou and S. H. Sun, *J Am Chem Soc*, 2007, 129, 8698-8699.

16.   B. B. M. Riskin, Y. Huang, and I. Willner, *Adv Mater*, 2007, 19, 2691-2695.

17.   J. D. Qiu, H. P. Peng, R. P. Liang and X. H. Xia, *Biosens Bioelectron*, 2010, 25, 1447-1453.

18.   G. Armelles, A. Cebollada, A. Garcia-Martin and M. U. Gonzalez, *Adv Opt Mater*, 2013, 1, 10-35.

19.   K. C. F. Leung, S. H. Xuan, X. M. Zhu, D. W. Wang, C. P. Chak, S. F. Lee, W. K. W. Ho and B. C. T. Chung, *Chem Soc Rev*, 2012, 41, 1911-1928.

20.   L. Y. Wang, J. Luo, Q. Fan, M. Suzuki, I. S. Suzuki, M. H. Engelhard, Y. H. Lin, N. Kim, J. Q. Wang and C. J. Zhong, *J Phys Chem B*, 2005, 109, 21593-21601.

21.   M. Piazza, M. Colombo, I. Zanoni, F. Granucci, P. Tortora, J. Weiss, T. Gioannini, D. Prosperi and F. Peri, *Angew Chem Int Edit*, 2011, 50, 622-626.

22.   J. Choi, S. Park, Z. Stojanovic, H. S. Han, J. Lee, H. K. Seok, D. Uskokovic and K. H. Lee, *Langmuir*, 2013, 29, 15698-15703.

23.   L. Y. Wang, J. Luo, M. M. Maye, Q. Fan, R. D. Qiang, M. H. Engelhard, C. M. Wang, Y. H. Lin and C. J. Zhong, *J Mater Chem*, 2005, 15, 1821-1832.

24.   W. Wu, Q. G. He and C. Z. Jiang, *Nanoscale Res Lett*, 2008, 3, 397-415.

25.   G. Mangiapia, G. Vitiello, C. Irace, R. Santamaria, A. Colonna, R. Angelico, A. Radulescu, G. D'Errico, D. Montesarchio and L. Paduano, *Biomacromolecules*, 2013, 14, 2549-2560.

26.   A. Lomakin, *Methods in Molecular Biology Amyloids Proteins*, Methods and Protocols, 2005.

27.   H. Zhang and O. Annunziata, *J Phys Chem B*, 2008, 112, 3633-3643.

28.   L. Paduano, R. Sartorio, G. D'Errico and V. Vitagliano, *J Chem Soc Faraday T*, 1998, 94, 2571-2576.

29.   A. Radulescu, V. Pipich, H. Frielinghaus and M. S. Appavou, *Sans-Yumo User Meeting at the Start-up of Scientific Experiments on the Ibr-2m Reactor: Devoted to the 75th Anniversary of Yu M Ostanevich's Birth*, 2012, 351.

30.   T. P. Russell, J. S. Lin, S. Spooner and G. D. Wignall, *J Appl Crystallogr*, 1988, 21, 629-638.

31.   P. Bartlett and R. H. Ottewill, *J Chem Phys*, 1992, 96, 3306-3318.

32.   J. S. B. Higgins, H. C., *Polymers and Neutron Scattering* Oxford Series on Neutron Scattering in Condensed Matter, 1997.

33.   P. D. Nellist and S. J. Pennycook, *Adv Imag Elect Phys*, 2000, 113, 147-203.

34.   *National Bureau of Standards (U. S.) Monograph*, 25 1967, 5.

35.   Swanson, *National Bureau of Standards (U. S.) Circ.*, 25, 1953, 13.

36.   M. M. Noginov, N. Noginova, O. Amponsah, R. Bah, R. Rakhimov and V. A. Atsarkin, *J Magn Magn Mater*, 2008, 320, 2228-2232.

37.   F. Bou-Abdallah and N. D. Chasteen, *J Biol Inorg Chem*, 2008, 13, 15-24.

38.   M. Fittipaldi, C. Innocenti, P. Ceci, C. Sangregorio, L. Castelli, L. Sorace and D. Gatteschi, *Phys Rev B*, 2011, 83, 104409-10.

39.   C. P. Bean and J. D. Livingston, *J Appl Phys*, 1959, 30, S120-S129.

TABLE OF CONTENTS GRAPHIC.